

Effects of Ternary Additions on the Microstructure and Thermal Stability of Directionally-Solidified MoSi₂/Mo₅Si₃ Eutectic Composites

Kosuke Fujiwara¹, Hirotaka Matsunoshita¹, Yuta Sasai¹, Kyosuke Kishida^{1,2,*} and Haruyuki Inui^{1,2}

¹ Department of Materials Science and Engineering, Kyoto University
Sakyo-ku, Kyoto 606-8501, Japan

² Center for Elements Strategy Initiative for Structural Materials (ESISM),
Kyoto University, Sakyo-ku, Kyoto 606-8501, JAPAN

*Corresponding author: Kyosuke KISHIDA

Department of Materials Science and Engineering,
Kyoto University, Sakyo-ku, Kyoto 606-8501, JAPAN

E-mail address: kishida.kyosuke.6w@kyoto-u.ac.jp

Tel.: +81-75-753-5461; fax: +81-75-753-5461

Abstract

Effects of ternary additions on the microstructure and thermal stability of directionally-solidified MoSi₂/Mo₅Si₃ eutectic composites have been studied for twelve different elements (Ti, V, Cr, Fe, Co, Ni, Nb, Ta, W, Ir, B and C) paying special attention to the variation of lattice misfits and interface segregation behavior with ternary additions. Among six elements (type-1: Ti, V, Cr, Nb, Ta and W) with a relatively high solubility in MoSi₂ and Mo₅Si₃, Ta and W are found to be beneficial to microstructure refinement. All other six ternary elements (type-2: Fe, Co, Ni, Ir, B and C) with a negligibly low solubility in MoSi₂ and Mo₅Si₃ exhibit a strong tendency to segregate on MoSi₂/Mo₅Si₃ interfaces, resulting in both microstructure refinement and the modification of the interface morphology.

Keywords: A. molybdenum silicides; B. alloy design, thermal stability, C. crystal growth; D. microstructure, phase interfaces;

1. Introduction

In recent years, there is a very strong demand for efficiency improvement of combustion systems for power plants and aircraft engines in order to reduce the consumption of fossil fuels and emission of greenhouse gases. One of the most effective ways to achieve this is to increase the operating temperature of gas turbine combustion systems, which currently achieve thermal efficiency about 40 % as stand-alone units and over 60 % when combining with steam turbine systems [1,2]. In the latest gas turbine systems with air-cooled turbine blades of Ni-based superalloys, the highest gas inlet temperature reaches to 1600 °C, which is more than 200 °C higher than the melting temperature of the superalloy used [1]. As far as the combustion system relies on the air-cooling of turbine blades, any drastic increase in the operating temperature (and therefore in the thermal efficiency) may not be expected. From this perspective, it is evident that a new class of ultra-high-temperature structural materials that can be used in the severe oxidizing atmosphere at temperatures beyond the maximum operating temperatures of Ni-based superalloys has to be developed. Transition-metal silicides have been considered as promising candidates for replacing Ni-based superalloys mainly because of their high melting temperature mostly more than 2000 °C and expected good oxidation resistance at high temperatures [3-5]. Among various transition-metal silicides, a considerable amount of attention has been paid to MoSi₂ with the tetragonal C11_b structure because of its high melting point (2020 °C), excellent high-temperature oxidation resistance and relatively low density [3-9]. Mechanical properties of MoSi₂, such as yield strength, fracture toughness and creep properties have been studied with the use of single crystals [7-11] and polycrystals [5,6]. Of particular interest is that in single crystals, plastic

flow is possible by dislocation motion even at and below room temperature depending on crystal orientation [7,9,10]. Nevertheless, poor fracture toughness of monolithic MoSi₂ around 3 MPa m^{1/2} at room temperature has remained as one of the drawbacks, together with insufficient strength of polycrystals at high temperatures [3-5,9]. Extensive studies have been made to improve these drawbacks in mechanical properties by forming composites with hard ceramics such as SiC, TiC, ZrO₂, TiB₂, Si₃N₄ through powder processing routes [3-5, 9, 12-13]. Although modest improvement in fracture toughness is reported to achieve by these composites, some of them are reported to suffer from pesting, which is catastrophic oxidation that occurs in the temperature range of 400 - 600 °C especially when they are less dense [3-5, 15-18]. Since pesting is known to be suppressed to occur in single crystals of MoSi₂ [15,16,18], MoSi₂-based single crystalline composites produced by ingot metallurgy routes are considered to have great advantages over polycrystalline composites produced by powder metallurgy routes.

MoSi₂/Mo₅Si₃ eutectic composites may be one of the promising candidates because of their high eutectic temperature (1900 °C for the binary alloy) and fine microstructures of the so-called script lamellar type formed simply by directional solidification (DS) [9,13,18-26]. Previous studies on MoSi₂/Mo₅Si₃ eutectic composites have revealed that the creep properties are much superior to those of other MoSi₂-based composites [21], while fracture toughness at room temperature for DS ingots of binary MoSi₂/Mo₅Si₃ eutectic composites is still insufficient [9, 13]. In the eutectic script lamellar structure in binary DS ingots, an orientation relationship of (110)_{MoSi₂}//(001)_{Mo₅Si₃} and [110]_{MoSi₂}//[110]_{Mo₅Si₃} is reported to occur between MoSi₂ and Mo₅Si₃ with a growth direction being nearly parallel to [110]_{MoSi₂} and [001]_{Mo₅Si₃} [20, 22]. Two different types of main interphase boundaries have been noted; one with (110)_{MoSi₂} // (110)_{Mo₅Si₃} and another inclined by about 15° from (001)_{MoSi₂} // (110)_{Mo₅Si₃} (see Fig. 1). Since MoSi₂ and Mo₅Si₃ both have body-centered tetragonal structures of C11_b and D8_m-types, respectively, there is a high probability to control the interfacial energy through changing lattice misfits between the two phases by alloying, by which fracture toughness of the composites may be improved. In addition, segregation of a particular alloying element on the interphase boundary, if it occurs, may also influence fracture toughness of the composites through changing the cohesive energy of the boundary, as frequently reported in many metallic materials such as iron [26, 27]. Since not only the microstructure but also the mechanical properties of MoSi₂/Mo₅Si₃ eutectic composites are thus expected to vary with ternary alloying through the changes in the interfacial energy, it is quite important to establish microstructure-property relationships in MoSi₂/Mo₅Si₃ eutectic composites upon ternary alloying. However, almost nothing is known about how the microstructure, its thermal stability and the resultant mechanical properties of MoSi₂/Mo₅Si₃ eutectic composites are affected by ternary alloying, except for Er- and Nb-alloyed MoSi₂/Mo₅Si₃ eutectic composites [20, 23].

In the present paper, we report the effects of ternary additions of twelve different elements (Ti, V, Cr, Fe, Co, Ni, Nb, Ta, W, Ir, B and C) on the microstructures and their thermal stability of DS ingots of MoSi₂/Mo₅Si₃ eutectic composites, paying special attention to microstructural changes due to variations of lattice misfits and segregation of ternary elements. This is a part of our investigation of microstructure-property relationships in MoSi₂/Mo₅Si₃ eutectic composites upon ternary alloying, and mechanical properties (yield strength, dislocation behavior and fracture toughness) of these ternary ingots will be published subsequently elsewhere.

2. Experimental procedures

Rod ingots of the binary alloy with a MoSi₂/Mo₅Si₃ eutectic composition of Mo - 54 at.%Si and ternary alloys with nominal compositions of Mo - 54 at.%Si - *x* at.%X (X = Ti, V,

Cr, Fe, Co, Ni, Nb, Ta, W and Ir, $x = 0.1 \sim 5$) and Mo - (54 - x) at.%Si - x at.%X (X = B and C, $x = 0.15 \sim 2$) were prepared by arc-melting. DS ingots were grown from the rod ingots using an optical floating-zone furnace at various growth rates ranging from 2 to 200 mm/h under an Ar gas flow. Average chemical compositions of all of the DS ingots were confirmed to be nearly identical to the nominal values with a minor deviation of less than about 1 at.%. Parts of the DS ingots were heat-treated at 1500 °C for 500h in vacuum. Microstructures of the DS and heat-treated ingots were examined by scanning electron microscopy (SEM) with a JEOL JSM-7001FA equipped with a field emission gun and by scanning transmission electron microscopy (STEM) with a JEOL JEM-2100F equipped with a field emission gun operated at 200 kV. Chemical compositions were analyzed by energy dispersive X-ray spectroscopy (EDS) in SEM and STEM. Lattice parameters for both phases in each alloy were determined by powder X-ray diffraction (XRD) method in order to estimate the lattice misfits at various MoSi₂/Mo₅Si₃ interfaces.

3. Results

3.1 Binary MoSi₂/Mo₅Si₃ eutectic composites

DS ingots of MoSi₂/Mo₅Si₃ eutectic composites generally exhibit a so-called script lamellar structure [20]. Detailed orientation analysis by XRD, SEM-EBSD and TEM has confirmed that MoSi₂ and Mo₅Si₃ phases in the script lamellar structure are grown nearly along [110]_{MoSi₂} and [001]_{Mo₅Si₃}, maintaining the orientation relationship of [110]_{MoSi₂} // [110]_{Mo₅Si₃} and (110)_{MoSi₂} // (001)_{Mo₅Si₃} with minor deviations of about 2°, as previously reported [20, 22].

SEM backscattered-electron images of three mutually orthogonal sections, cross ((110)_{MoSi₂} // (001)_{Mo₅Si₃}) and two longitudinal ((110)_{MoSi₂} // (110)_{Mo₅Si₃} and (001)_{MoSi₂} // (110)_{Mo₅Si₃}) sections of a DS ingot of a binary eutectic composite are shown in Figs. 1(a)-(c), respectively. Dark and bright regions in the figures correspond to MoSi₂ and Mo₅Si₃ phases, respectively. Approximate crystallographic orientations for these sections are indicated in the figure. Fine microstructure composed of a MoSi₂ matrix and an interconnected network of Mo₅Si₃ is developed with a macroscopic inclination of about 15° from the growth direction, as clearly seen in the (110)_{MoSi₂} // (110)_{Mo₅Si₃} longitudinal section of the DS composite (Fig. 1(b)).

From the microstructural characteristics, we have found that two types of interfaces, hereafter designated as interfaces I and II (Figs. 1 (j)-(l)), play important roles in determining the morphology and stability of microstructures. These two types of interfaces are perpendicular to each other in the (110)_{MoSi₂} // (001)_{Mo₅Si₃} cross section (Figs. 1 (a) and (j)). The interface I macroscopically inclined about 15° from the growth direction in the (110)_{MoSi₂} // (110)_{Mo₅Si₃} longitudinal section (Figs. 1 (b) and (k)), has been reported to possess the so-called ledge-terrace structure at the atomic scale [20, 22]. Approximate orientation relationships for the terrace and ledge parts of the interfaces I and II are described as follows.

Interface I, terrace part: (001)_{MoSi₂} // (110)_{Mo₅Si₃}^{*}, [110]_{MoSi₂} // [110]_{Mo₅Si₃},

Interface I, ledge part: (110)_{MoSi₂} // (001)_{Mo₅Si₃}^{*}, [110]_{MoSi₂} // [110]_{Mo₅Si₃},

Interface II: (110)_{MoSi₂} // (110)_{Mo₅Si₃}, [001]_{MoSi₂} // [110]_{Mo₅Si₃}^{*}.

The orientation relationships marked with asterisks are only approximate since slight misalignment is involved, details of which will be described later in this section.

With the orientation relationships described above, we have to consider three different types of lattice misfits, as proposed by Mason et al. [20]. These three types of lattice misfits are denoted as misfits A, B and C as defined with the following equations:

$$\text{Misfit A} = 2 \frac{d_{110 \text{ of MoSi}_2} - d_{330 \text{ of Mo}_5\text{Si}_3}}{d_{110 \text{ of MoSi}_2} + d_{330 \text{ of Mo}_5\text{Si}_3}} \quad (1a),$$

$$\text{Misfit B} = 2 \frac{d_{110 \text{ of MoSi}_2} - d_{002 \text{ of Mo}_5\text{Si}_3}}{d_{110 \text{ of MoSi}_2} + d_{002 \text{ of Mo}_5\text{Si}_3}} \quad (1b),$$

$$\text{Misfit C} = 2 \frac{d_{002 \text{ of MoSi}_2} - d_{220 \text{ of Mo}_5\text{Si}_3}}{d_{002 \text{ of MoSi}_2} + d_{220 \text{ of Mo}_5\text{Si}_3}} \quad (1c),$$

where $d_{hkl \text{ of MoSi}_2}$ and $d_{hkl \text{ of Mo}_5\text{Si}_3}$ indicate interplanar distances of $\{hkl\}$ planes in MoSi_2 and Mo_5Si_3 , respectively. Slight misalignment of about 2° between $[110]_{\text{MoSi}_2}$ and $[001]_{\text{Mo}_5\text{Si}_3}$ is neglected here for simplicity. As seen in Fig. 2, the stability of the interface I should be affected by all three kinds of lattice misfits A, B and C, while that of the interface II is affected by misfits B and C.

Figs. 3(a) and (b) show typical examples of atomic-resolution high-angle annular dark-field (HAADF)-STEM images of the interfaces I and II observed in a thin foil cut parallel to the $(110)_{\text{MoSi}_2} // (001)_{\text{Mo}_5\text{Si}_3}$ cross section in a DS ingot of a binary $\text{MoSi}_2/\text{Mo}_5\text{Si}_3$ eutectic composite grown at a growth rate of 10 mm/h. These images were taken along $[001]_{\text{Mo}_5\text{Si}_3}$, which is nearly parallel to $[110]_{\text{MoSi}_2}$ and the growth direction of the DS ingot. In the atomic-resolution HAADF-STEM images, atomic columns are imaged as bright spots, brightness of which is approximately proportional to the square of the average atomic number (Z) in the atomic columns. Because of relatively large atomic number difference between Mo (42) and Si (14), only the atomic columns of Mo are imaged for the Mo_5Si_3 phase in Figs. 3(a) and (b) with the STEM equipment used in this study. In MoSi_2 phase in Figs. 3(a) and (b) taken with the incident beam being parallel to $[001]_{\text{Mo}_5\text{Si}_3}$, atomic columns are not resolved and $(220)_{\text{MoSi}_2}$ planes are imaged as bright horizontal lines, clearly indicating that there exists slight misalignment between $[110]_{\text{MoSi}_2}$ and $[001]_{\text{Mo}_5\text{Si}_3}$, while $(110)_{\text{MoSi}_2}$ and $(110)_{\text{Mo}_5\text{Si}_3}$ are perfectly parallel to each other. Both interfaces are atomistically flat except for some regions corresponding to ledges as indicated by black arrowheads.

An atomic-resolution HAADF-STEM image and the corresponding selected-area electron diffraction (SAED) patterns taken from a region containing the interface I in the edge-on configuration are shown in Figs. 3(c) and (d). These observations were made with a thin foil cut parallel to the $(110)_{\text{MoSi}_2} // (110)_{\text{Mo}_5\text{Si}_3}$ longitudinal section in a DS ingot of a binary $\text{MoSi}_2/\text{Mo}_5\text{Si}_3$ eutectic composite grown at a growth rate of 10 mm/h. Atomic columns of pure Mo that appear as bright spots are clearly resolved both in MoSi_2 and in Mo_5Si_3 phases. This is consistent with the perfect alignment of $[110]_{\text{MoSi}_2}$ and $[110]_{\text{Mo}_5\text{Si}_3}$, both of which are parallel to the incident beam direction, although slight misalignment about 1.9° between $[110]_{\text{MoSi}_2}$ and $[001]_{\text{Mo}_5\text{Si}_3}$ is noted (Fig. 3(c) and (d)). The ledge-terrace structure described above is observed to be developed along the interface I shown in Fig. 3(c). These results are fully consistent with those previously reported [20, 22]. It is of importance to note that ledges with a height corresponding to the interplanar distance of $(110)_{\text{Mo}_5\text{Si}_3}$ are formed along the interface at an nearly regular interval, which is 13 times the interplanar distance of $(002)_{\text{Mo}_5\text{Si}_3}$ and 14 times that of $(110)_{\text{MoSi}_2}$, resulting in a macroscopic inclination about 13.5° of the

interface from $[110]_{\text{MoSi}_2}$. This is consistent with the inclination angle about 15° observed in the SEM images of the $(110)_{\text{MoSi}_2}/(110)_{\text{Mo}_5\text{Si}_3}$ longitudinal section (Fig. 1(b)).

The eutectic microstructure of binary DS ingots varies depending on the growth rate, as shown in Figs. 1(d)-(i). The binary DS ingot obtained at a growth rate of 50 mm/h (Figs. 1(d)-(f)) possesses a homogeneous and finer script lamellar structure when compared to that grown at a rate of 10 mm/h (Figs. 1(a)-(c)). However, when the growth rate is increased to 200 mm/h, a cellular structure appears instead of the homogenous script lamellar structure. In the cellular structure, much finer script lamellar structure and very coarse lamellar structure are developed at the center of the cell and the cell boundary regions, respectively. Such growth-rate dependence of the eutectic microstructures has generally been observed in many eutectic alloys grown in a range of growth condition called ‘coupled zone of eutectics’ [28, 29].

3.2 $\text{MoSi}_2/\text{Mo}_5\text{Si}_3$ eutectic composites with ternary additions

In the present study, the ternary elements added are found to be classified into two types according to their solubility in MoSi_2 and Mo_5Si_3 . Ternary elements, Ti, V, Cr, Nb, Ta and W that belong to groups 4 – 6 in the periodic table exhibit a relatively high solubility in MoSi_2 and Mo_5Si_3 , while the others (Fe, Co, Ni, Ir, B and C) possess a quite low solubility below 1 at.% [30, 31]. The former and latter are hereafter designated as type-1 and type-2 elements, respectively, and their microstructural variations will be described in the separate sections.

3.2.1 Ternary $\text{MoSi}_2/\text{Mo}_5\text{Si}_3$ eutectic composites with the type-1 elements (Ti, V, Cr, Nb, Ta and W)

3.2.1.1. Microstructure

As expected from relatively large solubilities of these ternary elements of the type-1 in MoSi_2 and Mo_5Si_3 in literature [30, 31], two-phase $\text{MoSi}_2/\text{Mo}_5\text{Si}_3$ eutectic microstructures are usually obtained without any ternary phase for all composites up to the 5 at.% addition, which corresponds to the maximum amount of ternary additions used in this study. However, microstructural characteristics vary depending on the ternary elements. SEM backscattered-electron images of the $(110)_{\text{MoSi}_2}/(001)_{\text{Mo}_5\text{Si}_3}$ cross section of ternary $\text{MoSi}_2/\text{Mo}_5\text{Si}_3$ DS ingots alloyed with 5 at.% Nb, Ta and W are shown in Figs. 4(a)-(c), respectively. All ingots were obtained at a growth rate of 10mm/h. DS ingots alloyed with Nb and Ta possess a homogeneous script lamellar structure when the amount of additions is small (less than 5 at.%), whereas when the amount of additions reaches 5 at.%, ingots tend to contain a small amount of an additional primary solidification phase (MoSi_2 (Fig. 4(a)) and Mo_5Si_3 (Fig. 4(b)) for Nb- and Ta-alloyed ingots, respectively). This may indicate the deviation of the eutectic composition from the Mo - 54 at.%Si composition upon alloying with a large amount of these elements, Nb and Ta. In contrast, DS ingots with W additions maintain a homogeneous script lamellar structure up to the 5 at.% addition. Microstructural characteristics in the homogeneous script lamellar structure in ternary DS ingots alloyed with Nb, Ta and W are virtually identical to those observed in the binary ingot grown at the same growth rate of 10 mm/h (Fig. 1(a)), except that Ta- and W-alloyed DS ingots possess a slightly finer microstructure than the binary DS ingot does.

In contrast, Ti-, V- and Cr-alloyed DS ingots exhibit a strong tendency to form a cellular eutectic structure with dispersed irregularity in microstructure when DS ingots are grown at a growth rate of 10 mm/h. Typical microstructures observed in the $(110)_{\text{MoSi}_2}/(001)_{\text{Mo}_5\text{Si}_3}$ cross section of DS ingots alloyed with various amounts of Ti, V and Cr grown at a growth rate of 10 mm/h are shown in Figs. 5(a)-(f). The cellular eutectic structure developed in DS ingots with 5 at.% additions of Ti (Fig. 5(b)) and V (Fig. 5(d)) and that with 1 at.% Cr (Fig. 5(e)) consists of a fine script lamellar structure at a central part of each columnar cell and a very

coarse and irregularly-shaped lamellar structure in cell boundary regions, while DS ingots with lesser amounts of Ti and V additions exhibit a relatively homogeneous script lamellar structure (Figs. 5(a) and (c)). Neither script lamellar structure nor cellular structure is observed any more in a 5 at.% Cr-alloyed DS ingot obtained at a growth rate of 10 mm/h (Fig. 5(f)) and a coarse and irregular eutectic structure is observed instead. Such variations in the eutectic structures are generally interpreted in terms of the degree of undercooling during solidification. It is well-known that the eutectic structure formed under a growth condition called ‘coupled zone of eutectics’ changes from planar eutectic structure to cellular eutectic, and to faceted eutectic dendrites with the increase in the growth rate (i.e., the degree of undercooling) [28, 29]. In the present eutectic composites, the planar eutectic structure corresponds to the homogeneous script lamellar structure. Since the growth rate is the same for all DS ingots shown in Figs. 5(a)-(f), the observed changes in the eutectic microstructure of Ti-, V- and Cr-alloyed DS ingots are considered to be caused by the relative increase in the degree of undercooling. In fact, the homogeneous script lamellar structure was obtained by reducing the amount of ternary addition and by decreasing the growth rate for Cr-alloyed DS ingots. For DS ingots alloyed with 1 at.% Cr, the cellular eutectic structure and homogeneous script lamellar structure are obtained when the growth rate is high (10 mm/h) and low (2 mm/h), as shown respectively in Figs. 5(e) and (g).

Although the microstructure of $\text{MoSi}_2/\text{Mo}_5\text{Si}_3$ eutectic composites varies with the growth rate, the microstructural variation of the homogeneous script lamellar structure with ternary additions is less pronounced when the microstructure in the $(110)_{\text{MoSi}_2}/(001)_{\text{Mo}_5\text{Si}_3}$ cross section of DS ingots is inspected (Figs. 4 and 5). This is also the case for the homogeneous script lamellar structure inspected in the $(110)_{\text{MoSi}_2}/(110)_{\text{Mo}_5\text{Si}_3}$ longitudinal section (Fig. 6). Flat portions that incline about 15° from the growth direction are maintained for the interface I in ternary DS ingots alloyed with 5 at.% V (Fig. 6(a)), 5 at.% Ta (Fig. 6(b)) and 2 at.% W (Fig. 6 (c)), although the extent of perturbation of the interface flatness varies somehow with ternary elements.

3.2.1.2. Partitioning behavior and lattice misfits

Chemical compositions of MoSi_2 , Mo_5Si_3 and some ternary phases evaluated in binary and ternary DS ingots by SEM-EDS are summarized in Table 1 for type-1 alloying elements. For all type-1 elements except for W, they are partitioned preferentially in the Mo_5Si_3 phase, while W is partitioned more or less evenly in MoSi_2 and Mo_5Si_3 phases.

Lattice parameters of the constituent phases in binary and some ternary DS ingots alloyed with type-1 elements estimated by the powder XRD method are also summarized in Table 1. Lattice constants of the MoSi_2 phase in DS ingots alloyed with these type-1 alloying elements are all identical with each other, reflecting the negligibly small solubility in MoSi_2 for Ti, V, Cr, Nb and Ta and the similarity in atomic radii for Mo (0.140 nm) and W (0.141 nm) [32]. In contrast, the Mo_5Si_3 phase exhibit relatively large variations in lattice parameters with ternary additions, trends of which can be interpreted primarily in terms of the difference in atomic radii between Mo and the corresponding ternary element. For Nb (0.147 nm) and Ta (0.147 nm) with an atomic radius larger than Mo, both *a*- and *c*-axis lattice parameters increase with the increase in the amount of ternary addition, while the opposite is the case for V (0.135 nm) and Cr (0.128 nm) with an atomic radius smaller than Mo. Additions of Ti (0.146 nm) result in an anisotropic expansion preferentially along the *a*-axis without any significant change along the *c*-axis. These results are well consistent with the previous report [33].

Values of lattice misfit for misfits A, B and C given in equations (1a)-(1c) are summarized in Fig. 7 as a function of the amount of alloying for type-1 alloying elements, based on the results summarized in Table 1. The absolute values of the lattice misfits A and B increase and

that of the lattice misfit C decreases with the increase in the amount of Nb and Ta additions. The completely opposite trend is observed for V and Cr additions, i.e., the absolute values of the lattice misfits A and B decrease and that of the lattice misfit C increases with the increase of their additions. On the other hand, Ti additions result in basically the same trend for the lattice misfits A and C as Nb and Ta additions, whereas the lattice misfit B is nearly unchanged because almost no change occurs in the *c*-axis lattice constant. Although changes in lattice misfit values upon alloying vary with ternary elements, the absolute values of lattice misfits of the three different types do not change significantly. The values of lattice misfits B and C remain high (about 8 and 14 %) with the change occurring in the range of 1 and 0.5 % upon alloying, whereas that of misfit A remain small (less than %) with the change in the range of 0.5 %. This may be one of the reasons why the flat portions with an inclination about 15° from the growth direction are maintained for the interface I irrespective of ternary elements, details of which are described later in the discussion section.

3.2.2 Ternary $\text{MoSi}_2/\text{Mo}_5\text{Si}_3$ eutectic composites with the type-2 elements (Fe, Co, Ni, Ir, B, C)

3.2.2.1 Microstructure

SEM backscattered-electron images of the $(110)_{\text{MoSi}_2}/(001)_{\text{Mo}_5\text{Si}_3}$ cross section of ternary $\text{MoSi}_2/\text{Mo}_5\text{Si}_3$ DS ingots alloyed with 2 at.% Fe, Co, Ni, 0.2 at.% Ir, 2 at.% B and 1 at.% C (type-2 elements) grown at a growth rate of 10 mm/h are shown in Fig. 8. As seen in Table 2 which summarizes chemical compositions of MoSi_2 , Mo_5Si_3 and some ternary phases in the ternary DS ingots containing type-2 alloying elements, the solid solubilities of these type-2 alloying elements in both the MoSi_2 and Mo_5Si_3 phases are all negligibly small. A very coarse and irregularly-shaped eutectic structure is observed in Fe-, Co-, Ni- and Ir-alloyed DS ingots accompanied by the formation of an additional ternary phase on some of the $\text{MoSi}_2/\text{Mo}_5\text{Si}_3$ interfaces (Figs. 8(a)-(d)). Ternary phases in DS ingots alloyed with Fe, Co, Ni and Ir are inferred respectively to be MoFe_2Si_2 or MoFe_2 , MoCoSi , MoNiSi and IrSi based on the chemical composition revealed by EDS and previously reported phase diagrams [31]. The B-alloyed DS ingots exhibits a cellular structure similar to those observed in DS ingots with additions of 5 at.% V and Ti (Fig. 6). An additional ternary phase is also noted to form on some of the $\text{MoSi}_2/\text{Mo}_5\text{Si}_3$ interfaces as clearly seen at a higher magnification (Fig. 8(f)). The ternary phase in the DS ingot alloyed with B is similarly inferred to be MoB [31]. On the other hand, the C- alloyed DS ingot exhibits a homogeneous script lamellar structure, although an additional ternary phase, which is inferred to be $\text{Mo}_5\text{Si}_3\text{C}$ [31], is also noted to form on some of the $\text{MoSi}_2/\text{Mo}_5\text{Si}_3$ interfaces as clearly seen at a higher magnification (Fig. 8(g) and (h)).

These ternary phases usually observed in DS ingots alloyed with type-2 alloying elements can be eliminated by decreasing the amounts of these additions to less than 0.2 at.%. Typical examples of the homogeneous script lamellar structure observed in the $(110)_{\text{MoSi}_2}/(001)_{\text{Mo}_5\text{Si}_3}$ cross section and $(110)_{\text{MoSi}_2}/(110)_{\text{Mo}_5\text{Si}_3}$ and $(001)_{\text{MoSi}_2}/(110)_{\text{Mo}_5\text{Si}_3}$ longitudinal sections of DS ingots alloyed with 0.1 at.% Co, 0.16 at.% B (=300 wt.ppm B) and 0.15 at.% C (=300 wt.ppm C) are shown in Fig. 9. It is easily recognized that the ternary phases are completely eliminated from the ingots and that the homogeneous script lamellar structures observed in the $(110)_{\text{MoSi}_2}/(001)_{\text{Mo}_5\text{Si}_3}$ cross section of the ternary ingots are finer than that observed in binary DS ingots (Figs. 1(a)-(c)) obtained at the same growth rate of 10 mm/h. On top of that, these ternary DS ingots alloyed with 0.1 at.% Co, 0.16 at.% B and 0.15 at.% C lose almost all flat portions of the interface I (evident when viewed in the $(110)_{\text{MoSi}_2}/(110)_{\text{Mo}_5\text{Si}_3}$ longitudinal section; Figs. 9(b), (e) and (h)).

3.2.2.2. Interface segregation of the ternary elements of type 2

Because of the negligibly small solubility of type-2 elements in the MoSi_2 and Mo_5Si_3 phases, segregation of these alloying elements on the $\text{MoSi}_2/\text{Mo}_5\text{Si}_3$ interface is expected. Chemical compositions across the $\text{MoSi}_2/\text{Mo}_5\text{Si}_3$ interface were analyzed by STEM-EDS using thin foils cut parallel to the $(110)_{\text{MoSi}_2}/(001)_{\text{Mo}_5\text{Si}_3}$ cross section, in order to investigate the segregation behavior of some of type-2 elements. Figs. 10(a) and (b) show the results of EDS analysis made respectively for the interfaces I and II in a DS ingot alloyed with 0.5at.% Co grown at a rate of 10 mm/h. Significant segregation of Co is clearly seen to occur on both types of interfaces, so that the chemical composition of Co on the interface is as high as 3 to 5 times that of the Mo_5Si_3 matrix. Segregation of Ni and Ir is similarly observed to occur on both types of interfaces, as shown in Figs. 10(c) and (d). Variations of chemical compositions across the interface I in a DS ingots alloyed with 0.5 at.% Ni were inspected by STEM-EDS, as shown in Fig. 11. Although the flat portions (inclined by 15° from the growth direction in the binary counterpart) of the interface I are almost completely lost upon alloying with type-2 elements (Fig. 9), portions corresponding to the ledge and terrace parts are observed still to exist without having any regularity for their arrangement, as clearly seen in an atomic-scale image shown in Fig. 11(a). The extent of segregation of Ni exactly on the boundary is much higher in the ledge portion than in the terrace portion (Fig. 11(c)). Similar anisotropic segregation behaviors were observed also for DS ingots alloyed with Co and Ir. We expect a similar anisotropic segregation behaviors for other type-2 alloying elements, when judged from the similar tendency in the solid solubility in the MoSi_2 and Mo_5Si_3 phases and the microstructure variation upon alloying.

3.3. Thermal stability of microstructure

In order to confirm the thermal stability of the eutectic microstructure, annealing experiments were made for various DS ingots at 1500°C for 500h in vacuum. No apparent changes in microstructure were detected for all DS ingots examined, indicating the very high thermal stability of the $\text{MoSi}_2/\text{Mo}_5\text{Si}_3$ eutectic microstructure even at a very high temperature of 1500°C .

4. Discussion

4.1. Relationship between lattice misfits and interface structure

In the script lamellar structure of binary two-phase $\text{MoSi}_2/\text{Mo}_5\text{Si}_3$ eutectic composites, a characteristic ledge-terrace structure is observed to form at the interface I. The ledge-terrace structure of the interface I is revealed through atomic-resolution HAADF-STEM imaging to consist of regularly-spaced ledges with a fixed height corresponding to the interplanar distance of $(110)_{\text{Mo}_5\text{Si}_3}$. Since a ledge-terrace structure is generally considered to form to accommodate lattice misfits between two phases in a particular orientation relationship [34, 35], it should be important to consider the relationship between the observed interface microstructure and the misfit accommodation. For simplicity, we consider here two types of lattice misfits B and C, which correspond primarily to those at the terrace and ledge parts of the interface I, respectively. Since the absolute value of the misfit C ($\sim 13\%$ for the binary alloy) is larger than that of the misfit B ($\sim 8\%$), the accommodation for the misfit C is considered first. Figure 12 schematically illustrates misfit accommodation achieved by tilting one of the two crystals with respect to the other across the interface. As shown in Fig. 12(b), if a small tilt (with the angle ϕ) is introduced for one of the two crystals (Mo_5Si_3 in this case), the lattice misfit C is eliminated on the interface labeled OP, which is inclined both from $(001)_{\text{MoSi}_2}$ and from $(110)_{\text{Mo}_5\text{Si}_3}$. Such a macroscopic inclination of the interface I through the introduction of a ledge-terrace structure (Fig. 12(c)) is indeed observed to occur in the script lamellar structure of binary two-phase $\text{MoSi}_2/\text{Mo}_5\text{Si}_3$ eutectic composites (Figs. 1(b), (e) and

(h)). The angle θ for the macroscopic inclination of the interface I from $(001)_{\text{MoSi}_2}$ is correlated with the tilt angle ϕ with the following equation.

$$\tan \theta = \frac{d_{001 \text{ of MoSi}_2} \cdot \sin \phi}{d_{001 \text{ of MoSi}_2} \cdot \cos \phi - d_{110 \text{ of Mo}_5\text{Si}_3}} \quad (2).$$

In the case of the interface I formed during solidification, the interface inclination angle must be determined so as to minimize the misfit strain related not only to the misfit C but also to the misfit B. The misfit strain related to the misfit B is expected to be minimized when the following relation is satisfied, in addition to the equation (2).

$$(m \cdot d_{110 \text{ of MoSi}_2})^2 + (d_{001 \text{ of MoSi}_2})^2 = (n \cdot d_{002 \text{ of Mo}_5\text{Si}_3})^2 + (d_{110 \text{ of Mo}_5\text{Si}_3})^2 \quad (3),$$

where m and n are integers. If m is equal to n , no misfit strain remains macroscopically at the interface. If m is not equal to n , a semi-coherent interface containing a single set of interface dislocations with a regular interval is formed. However, that the equation (3) is not exactly satisfied with integer values for m and n , because of the lattice parameters for MoSi_2 and Mo_5Si_3 . Approximate solutions can be found by plotting the left and right sides of the equation (3) as a function of the tilt angle ϕ . This is done in Fig. 13(a) with the use of the lattice parameters for binary MoSi_2 ($a_{\text{MoSi}_2} = 0.321$ nm, $c_{\text{MoSi}_2} = 0.785$ nm) and Mo_5Si_3 ($a_{\text{Mo}_5\text{Si}_3} = 0.966$ nm, $c_{\text{Mo}_5\text{Si}_3} = 0.490$ nm) at room temperature (Table 1). The expected tilt angle ϕ can be estimated from the following equations.

$$m \cdot d_{110 \text{ of MoSi}_2} = \frac{d_{001 \text{ of MoSi}_2} \cdot \cos \phi - d_{110 \text{ of Mo}_5\text{Si}_3}}{\sin \phi} \quad (4a),$$

$$n \cdot d_{002 \text{ of Mo}_5\text{Si}_3} = \frac{d_{001 \text{ of MoSi}_2} - d_{110 \text{ of Mo}_5\text{Si}_3} \cdot \cos \phi}{\sin \phi} \quad (4b).$$

Inspection of the figure reveals that the values of the left and right sides of equation (3) almost coincide with each other at a tilt angle about 1.71° , at which m and n are 15 and 14, respectively. The macroscopic inclination angle θ of the interface I from $(001)_{\text{MoSi}_2}$ is then calculated to be about 13.0° . These values are quite close to those experimentally observed in Figs. 1(b), 3(c) and 3(d), where m , n , ϕ and θ are 14, 13, 1.9° and 13.5° , respectively. Slight differences for values of m and n are considered to reflect the difference in the lattice parameters between room temperature and the eutectic temperature of 1900°C . If we assume that coefficients for linear thermal expansion for MoSi_2 and Mo_5Si_3 [36, 37] are constant up to the eutectic temperature, the lattice parameters for binary MoSi_2 and Mo_5Si_3 at the eutectic temperature can be estimated to be $a_{\text{MoSi}_2} = 0.326$ nm, $c_{\text{MoSi}_2} = 0.799$ nm and $a_{\text{Mo}_5\text{Si}_3} = 0.975$ nm, $c_{\text{Mo}_5\text{Si}_3} = 0.501$ nm, respectively. With the use of these lattice parameters, the values m , n , ϕ and θ are calculated to be 14, 13, 1.93° and 13.9° , respectively, which are almost perfectly consistent with those experimentally observed. We can thus conclude that the $\text{MoSi}_2/\text{Mo}_5\text{Si}_3$ eutectic microstructure grows so as to minimize the misfit strain at the interface I during solidification.

We now evaluate how the lattice misfits affect the interface structure and morphology of the interface I in DS ingots alloyed with type-1 elements by estimating the values m , n , ϕ and θ with the lattice parameters determined for ternary elements of type-1 (Table 1). The evaluation was made for DS ingots with additions of 5 at.% V and 5 at.% Ta, since relatively large changes in lattice misfits are observed upon alloying with these elements (Fig. 4). The results of the evaluation for the V-alloyed and Ta-alloyed DS ingots are shown in Figs. 13(b) and (c), respectively. The values of m , n , ϕ and θ for the 5 at.%-V alloyed DS ingot are estimated respectively to be 16, 15, 1.64° and 12.2° , while those for the 5 at.%-Ta alloyed one are 14, 13, 1.77° and 13.9° . These values are not so much different from those calculated

for the binary counterpart. This is consistent with the fact that no significant change in the morphology of the flat portions of the interface I is noted upon alloying with type-1 alloying elements (Fig. 7).

Although the lattice misfits induced by ternary alloying do not alter significantly the morphology of the interface I in DS ingots alloyed with type-1 elements, the interface energy is expected to change upon alloying through the changes in the values m and n . This is because the difference in number between m and n corresponds to the number of interfacial dislocations (with the extra-half plane on the MoSi_2 side when $m > n$) in a terrace part of the interface I (Fig. 12(c)), since m and n are the numbers of $(110)_{\text{MoSi}_2}$ and $(002)_{\text{Mo}_5\text{Si}_3}$ atomic planes in the terrace part. If the number difference between m and n is one, each terrace contains single interfacial dislocation, and the interval of interfacial dislocations in that case is identical with the length of each terrace, which corresponds to the value of m (or n). The interfacial energy is expected to increase with the increase in the interfacial dislocation density (i.e., with the decrease in the interval of interfacial dislocations). For all three different alloys shown in Fig. 13, the number difference between m and n is one. The interfacial dislocation density in the interface I is thus basically determined by the value of m (or n). We thus expect the highest interfacial energy for the 5 at.% Ta-alloyed DS ingot (Fig. 13(c); $m = 14$) of the three alloys while the lowest energy for the 5 at.% V-alloyed DS ingot (Fig. 13(c); $m = 16$). Our preliminary results indeed indicate that the Ta-alloyed DS ingots exhibit the highest propensity for delamination along the interface I on fracture toughness evaluation with an indentation fracture method. This result suggests the possibility that the fracture toughness of $\text{MoSi}_2/\text{Mo}_5\text{Si}_3$ eutectic composites can be improved by increasing the interfacial energy through lattice misfit control by alloying type-1 elements such as Ta and W. Fracture toughness improvement of $\text{MoSi}_2/\text{Mo}_5\text{Si}_3$ eutectic composites through interfacial energy control is currently under survey in our group.

4.2. Relationship between segregations of ternary elements and microstructures

Alloying elements of the type 2 (such as Co, Ni and Ir) that have a negligibly low solubility in both MoSi_2 and Mo_5Si_3 phases exhibit a strong tendency to segregate on the $\text{MoSi}_2/\text{Mo}_5\text{Si}_3$ interface in the homogeneous script lamellar structure of MoSi_2 and Mo_5Si_3 eutectic composites. In general, the stability of interphase boundaries is discussed in terms of the interfacial energy, which can be divided into the elastic term due to the lattice misfits and the chemical term due to atomic bonding across the interface. Since the solid-solubility of type-2 elements in both MoSi_2 and Mo_5Si_3 phases is negligibly small, changes in the elastic term of the interfacial energy is expected to be very small in ternary $\text{MoSi}_2/\text{Mo}_5\text{Si}_3$ eutectic composites alloyed with type-2 elements, when compared with the binary counterpart. Thus, the change in the chemical interaction energy across the interface is considered to play a dominant role in modifying the morphology (i.e., in losing the flat portions) (Figs. 8(b), 8(e) and 8(h)) of the interface I in $\text{MoSi}_2/\text{Mo}_5\text{Si}_3$ eutectic composites alloyed with type-2 elements. In fact, segregation of Ni (and Co, and Ir) on the $\text{MoSi}_2/\text{Mo}_5\text{Si}_3$ interphase boundary is observed to occur with the extent of segregation being more significant in the ledge part than in terrace part of the interface I (Fig. 11). Segregation of these elements is considered to result in lowering the interfacial energy, which occurs more effectively in the ledge part than in terrace part of the interface I, causing a decrease in the relative energy difference between ledge and terrace parts. We believe that such a decrease in the relative energy difference between ledge and terrace parts is responsible for the observed loss of the flat portions of the interface I. The interfacial energy caused by the segregation of the type-2 elements is also considered play an important role for the interlamellar spacing in the script-lamellar structure. According to the simple thermodynamic estimation by Zener [38], minimum interlamellar spacing is proportional to the interfacial energy and inversely proportional to the degree of undercooling. Since the slight ternary addition of the type-2 elements is not likely to alter the

degree of undercooling much in the cases of the DS alloys with the type-2 elements, the observed finer lamellar spacing is considered to be mainly affected by the lower interfacial energy caused by the segregation of the type-2 elements. The ternary addition of the type-2 elements is thus effective for fabricating finer microstructure, which is expected to be beneficial in improving mechanical properties of the DS eutectic ingots, especially for high temperature strength.

5. Conclusions

1. The microstructure of directionally-solidified $\text{MoSi}_2/\text{Mo}_5\text{Si}_3$ eutectic composites varies depending on the degree of undercooling, which can be controlled by changing the growth rate, and the ternary addition. The eutectic structure changes from planar eutectic (homogeneous script lamellar) to cellular eutectic, and to faceted eutectic dendrites with the increase in the growth rate or the degree of undercooling.
2. Among six type-1 elements (Ti, V, Cr, Nb, Ta and W) with a relatively high solubility in MoSi_2 and Mo_5Si_3 , microstructure refinement is achieved by additions of Ta and W. Although the morphology of flat portions of the interface I (with an inclination about 15° from the growth direction) in the homogeneous script lamellar structure is not significantly altered upon alloying these elements, the interface energy is considered to change upon alloying through the changes in lattice misfits, i.e., the numbers of $(110)_{\text{MoSi}_2}$ and $(002)_{\text{Mo}_5\text{Si}_3}$ atomic planes in the terrace part of the ledge-terrace structure of the interface I.
3. A strong segregation on the interphase boundary is noted for type-2 alloying elements (Fe, Co, Ni, Ir, B, C) whose solubility in MoSi_2 and Mo_5Si_3 is negligibly small. As a result, microstructure refinement occurs upon alloying with these elements at a very small level of alloying additions (less than about 0.1 ~ 0.16 at.%). The observed loss of the flat portions of the interface I in the homogeneous script lamellar structure is considered to occur due to the fact that the interface energy is reduced by segregation of type-2 alloying elements.
4. The eutectic structure developed during directional solidification is stable after heat treatment at 1500°C and for 500 hours, irrespective ternary elements.

Acknowledgements

This work was supported by the Advanced Low Carbon Technology Research and Development Program (ALCA) from the Japan Science and Technology Agency (JST) and in part by the Elements Strategy Initiative for Structural Materials (ESISM) from the Ministry of Education, Culture, Sports, Science and Technology (MEXT), Japan, and in part by JSPS KAKENHI (Nos. 24246113 and 25630304).

References

1. S. Hada, K. Tsukagoshi, J. Masada, E. Ito, Test results of the world's first $1,600^\circ\text{C}$ J-series gas turbine, *Mitsubishi Heavy Ind. Tech. Rev.*, 49 (2012) 18-23.
2. G.G. Ol'khovskii, Prospective gas turbine and combined cycle units for power engineering (a review), *Therm. Eng.*, 60 (2013) 79-88.
3. A.K. Vasudevan, J.J. Petrovic, A comparative overview of molybdenum disilicide composites, *Mater. Sci. Eng.*, A155 (1992) 1-17.
4. J.J. Petrovic, A.K. Vasudevan, Key developments in high temperature structural silicides, *Mater. Sci. Eng.*, A261 (1999) 1-5.
5. R. Mitra, Mechanical behaviour and oxidation resistance of structural silicides, *Int. Mater. Rev.*, 51 (2006) 13-64.
6. S.A. Maloy, A. H. Heuer, J.J. Lewandowski, T.E. Mitchell, On the slip systems in MoSi_2 , *Acta metal. mater.* 40 (1992) 3159-3165.
7. K. Ito, H. Inui, Y. Shirai, M. Yamaguchi, Plastic deformation of MoSi_2 single crystals, *Philos. Mag. A*, 72 (1995) 1075-1097.

8. S.A. Maloy, T.E. Mitchell, A. H. Heuer, High temperature plastic anisotropy in MoSi₂ single crystals, *Acta metal. mater.*, 43 (1995) 657-668.
9. K. Ito, T. Yano, T. Nakamoto, M. Moriwaki, H. Inui, M. Yamaguchi, Microstructure and mechanical properties of MoSi₂ single crystals and directionally solidified MoSi₂-based alloys, *Prog. Mater. Sci.*, 42 (1997) 193-207.
10. H. Inui, K. Ishikawa, M. Yamaguchi, Effects of alloying elements on plastic deformation of single crystals of MoSi₂, *Intermet.*, 8 (2000) 1131-1145.
11. H. Inui, K. Ishikawa, M. Yamaguchi, Creep deformation of single crystals of binary and some ternary MoSi₂ with the C11_b structure, *Intermet.*, 8 (2000) 1159-1168.
12. P. J. Meschter, D.S. Schwartz, Silicide-matrix materials for high-temperature applications, *JOM*, 41(11) (1989) 52-55.
13. K. Ito, T. Yano, T. Nakamoto, H. Inui, M. Yamaguchi, *Intermet.*, 4 (1996) S119-S131.
14. R. Gibala, A.K. Ghosh, D.C. Van Aken, D.J. Srolovitz, A. Basu, H. Chang, D.P. Mason, W. Yang, *Mater. Sci. Eng.*, A155 (1992) 147-158.
15. J.B. Berkowitz-Mattuck, P.E. Blackburn, E.J. Felten, The intermediate-temperature oxidation behavior of molybdenum disilicide, *Trans. Metall. Soc. AIME*, 233 (1965) 1093-1099.
16. J.B. Berkowitz-Mattuck, M. Rossetti, D.W. Lee, Enhanced oxidation of molybdenum disilicide under tensile stress: relation to pest mechanisms, *Metall. Trans.*, 1 (1970) 479-483.
17. P.J. Meschter, Low-temperature oxidation of molybdenum disilicide, *Metall. Trans. A*, 23A (1992) 1763-1772.
18. F. Zhang, L. Zhang, A. Shan, J. Wu, Oxidation of stoichiometric poly- and single-crystalline MoSi₂ at 773K, *Intermet.* 14 (2006) 406-411.
19. D. P. Mason, D.C. Van Aken, The effect of microstructural scale on hardness of MoSi₂-Mo₅Si₃ eutectics, *Scr. Metal. Mater.*, 28 (1993) 185-189.
20. D. P. Mason, D. C. Van Aken, J. F. Mansfield, On the microstructure and crystallography of directionally solidified MoSi₂-Mo₅Si₃ eutectics, *Acta metall. mater.*, 43 (1995) 1189-1199.
21. D. P. Mason, D.C. Van Aken, On the creep of directionally solidified MoSi₂-Mo₅Si₃ eutectics, *Acta metall. mater.*, 43 (1995) 1201-1210.
22. S.Q. Xiao, S.A. Maloy, A.H. Heuer, U. Dahmen, Morphology and interface structure of Mo₅Si₃ precipitates in MoSi₂, *Philos. Mag.*, 72 (1995) 997-1013.
23. S. Ueno, T. Fukui, R. Tanaka, S. Miura, Y. Mishima, Phase transformation of MoSi₂ phase in MoSi₂/Mo₅Si₃ eutectic alloy containing Nb, *Mater. Trans.*, 40 (1999) 369-372.
24. K. Fujiwara, Y. Sasai, K. Kishida, H. Inui, Effects of Ternary Additions on the Microstructure of Directionally-Solidified MoSi₂/Mo₅Si₃ Eutectic Composites, *MRS Symp. Proc.*, 1516 (2013) 189-194.
25. Y. Sasai, A. Inoue, K. Fujiwara, K. Kishida, H. Inui, Plastic Deformation of Directionally-Solidified MoSi₂/Mo₅Si₃ Eutectic Composites, *MRS Symp. Proc.*, 1516 (2013) 195-200.
26. C.J. McMahon Jr., V. Vitek, The effects of segregated impurity on intergranular fracture energy, *Acta Metall.*, 27 (1979) 507-513.
27. M.L. Jokl, V. Vitek, C.J. McMahon Jr., A microscopic theory of brittle fracture in deformable solids: a relation between ideal work to fracture and plastic work, *Acta Metall.*, 28 (1980) 1479-1488.
28. W. Kurz, D. J. Fisher, *Fundamentals of solidification*, fourth rev. ed., Trans Tech Publ., Switzerland, 1998.
29. J. LLorca, V.M. Orera, Directionally solidified eutectic ceramic oxides, *Prog. Mater. Sci.*, 51 (2006) 711-809.

30. D. Yi, Z. Lai, C. Li, O.M. Akselsen, J.H. Ulvensoen, Ternary alloying study of MoSi₂, Metall. Mater. Trans. A, 29A (1998) 119-129.
31. P. Villars, H. Okamoto, K. Cenzual (Eds.), ASM Alloy Phase Diagram Database, ASM Int., Materials Park, 2006-2013.
<<http://www1.asminternational.org/AsmEnterprise/APD>>.
32. E. Teatum, K. Gschneidner, Jr., J. Waber, Los Alamos Sci. Lab. Rep. LA-2345, U.S. Dep Commer, Washington D.C., 1960.
33. J.H. Schneibel, C.J. Rawn, T.R. Watkins, E.A. Payzant, Thermal expansion anisotropy of ternary molybdenum silicides based on Mo₅Si₃, Phys. Rev. B, 65 (2002) 134112-1-5.
34. J.H. van der Merwe, G.J. Shiflet, P.M. Stoop, Structural ledges in interphase boundaries, Metall. Trans. A, 22A (1991) 1165-1175.
35. Y. Mou, Intrinsic ledges at interphase boundaries and the crystallography of precipitate plates, Metall. Trans. A, 25A (1994) 1905-1915.
36. O. Thomas, J.P. Senateur, R. Madar, O. Laborde, E. Rosencher, Molybdenum disilicide: crystal growth, thermal expansion and resistivity, Solid State Commun., 55 (1985) 629-632.
37. F. Chu, D.J. Thoma, K. McClellan, P. Peralta, Y. He, Synthesis and properties of Mo₅Si₃ single crystals, Intermet., 7 (1999) 611-620.
38. C. Zener, Kinetics of the Decomposition of Austenite, Trans. A.I.M.E., 167 (1946) 550-583.

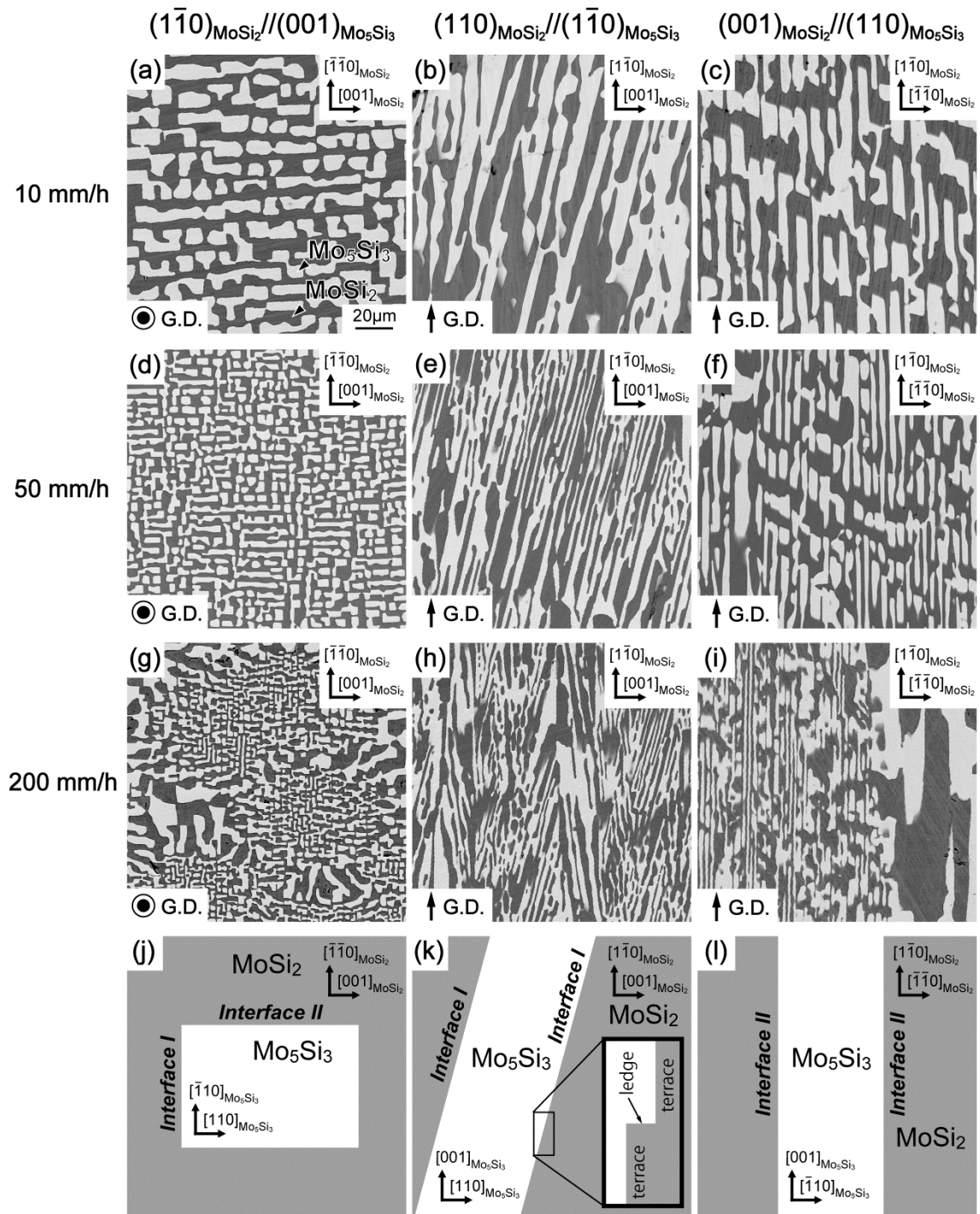


Fig. 1. (a-i) SEM backscattered electron images of three mutually orthogonal sections of DS ingots of binary MoSi₂/Mo₅Si₃ eutectic composites grown at growth rates of (a-c) 10 mm/h, (d-f) 50 mm/h and (g-i) 200 mm/h. (j-l) Schematic illustration of two types of interfaces between MoSi₂ and Mo₅Si₃ phases in the eutectic composites.

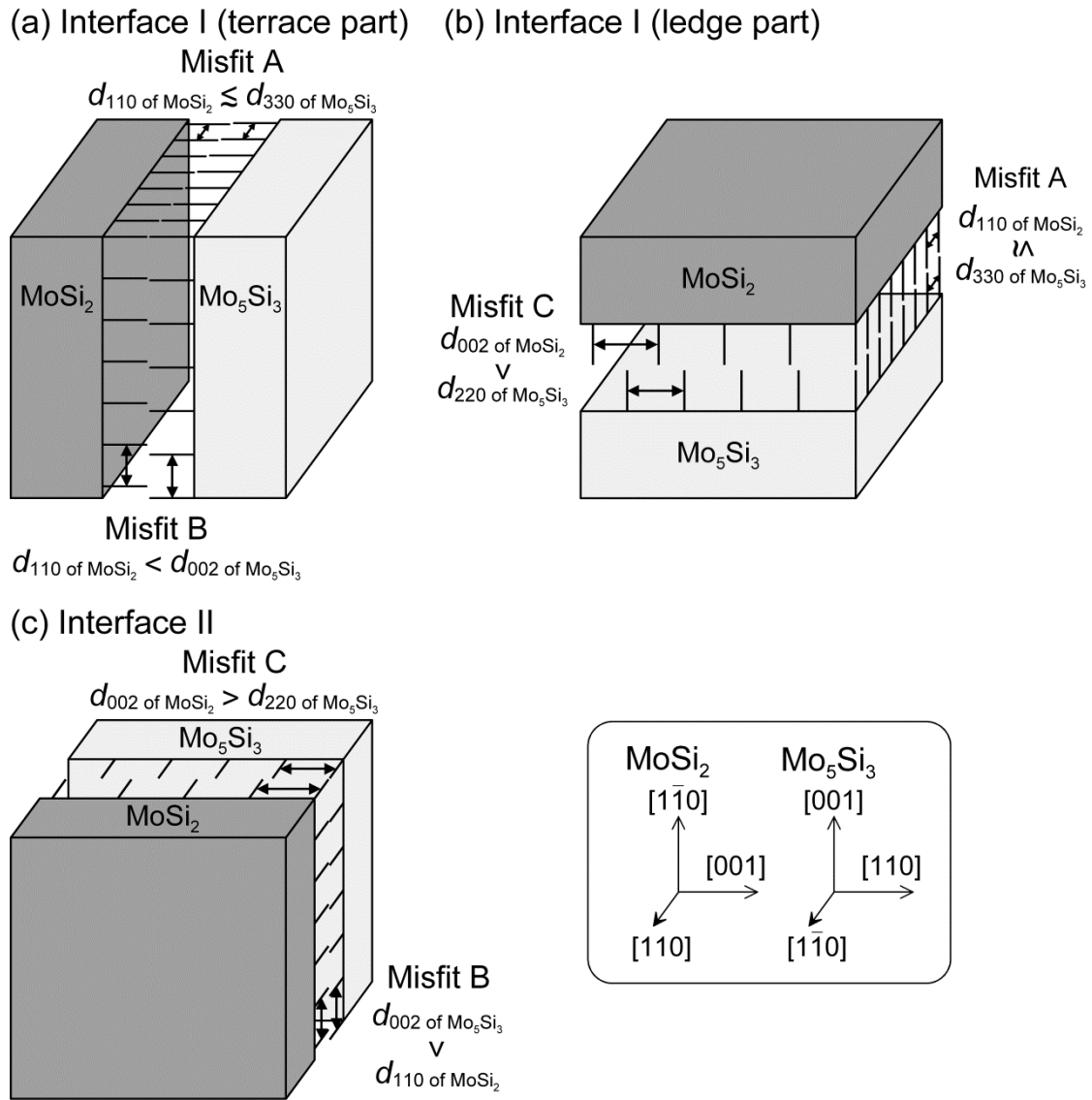


Fig. 2 Schematic illustrations of three types of interfaces and corresponding lattice misfits in $\text{MoSi}_2/\text{Mo}_5\text{Si}_3$ eutectic composites.

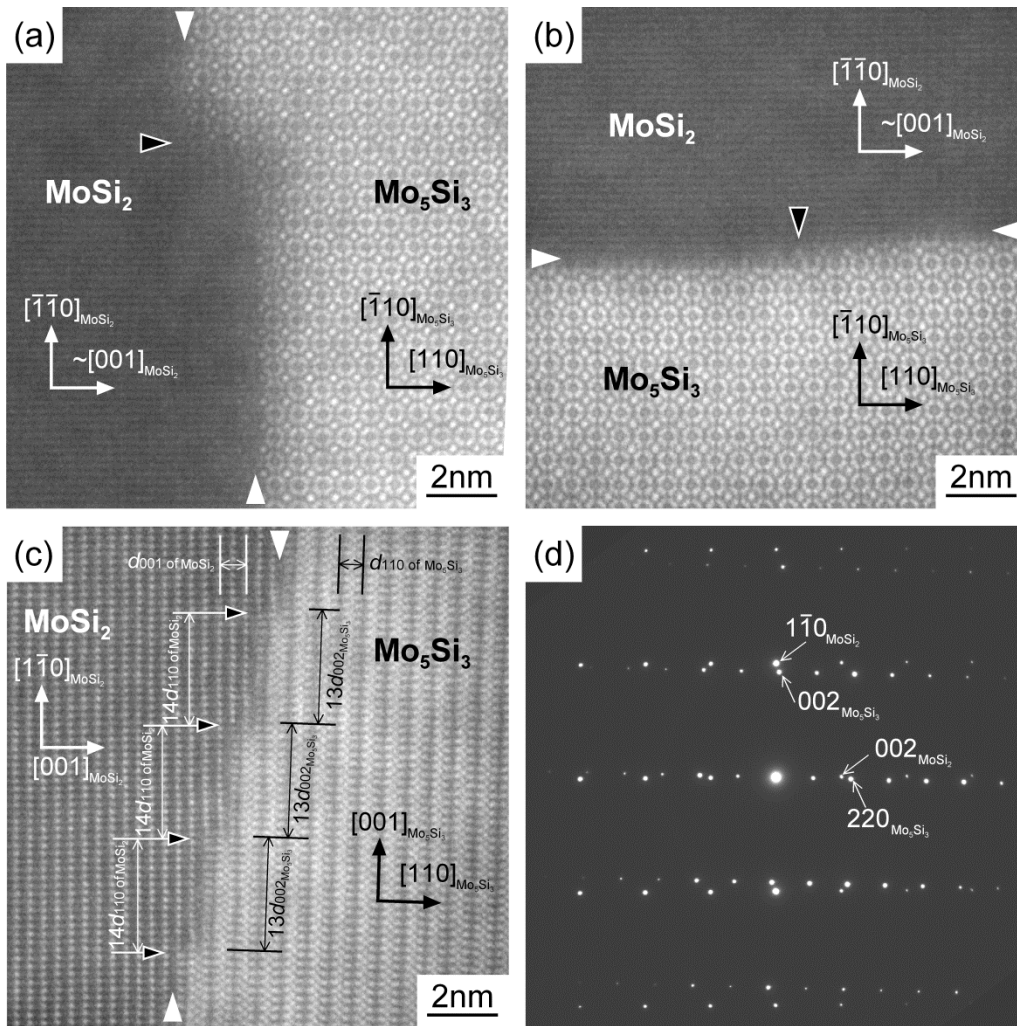


Fig. 3. Atomic resolution HAADF-STEM images and a selected area electron diffraction patterns taken from the interface region in a binary DS ingot grown at a growth rate of 10 mm/h projected along (a),(b) $[001]_{\text{Mo}_5\text{Si}_3}$ and (c),(d) $[110]_{\text{MoSi}_2}/[110]_{\text{Mo}_5\text{Si}_3}$.

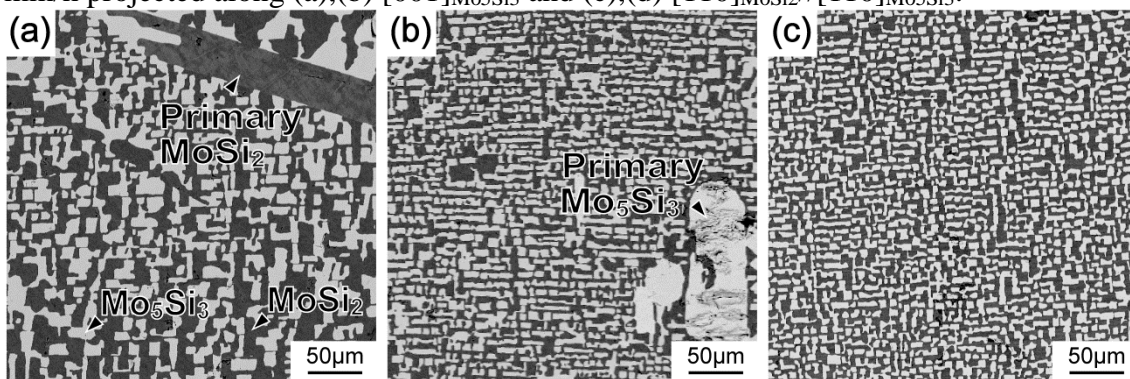


Fig. 4. SEM backscattered electron images of cross sections of DS $\text{MoSi}_2/\text{Mo}_5\text{Si}_3$ eutectic composites alloyed with (a) 5 at.% Nb, (b) 5 at.% Ta and (c) 5 at.% of W grown at a growth rate of 10mm/h.

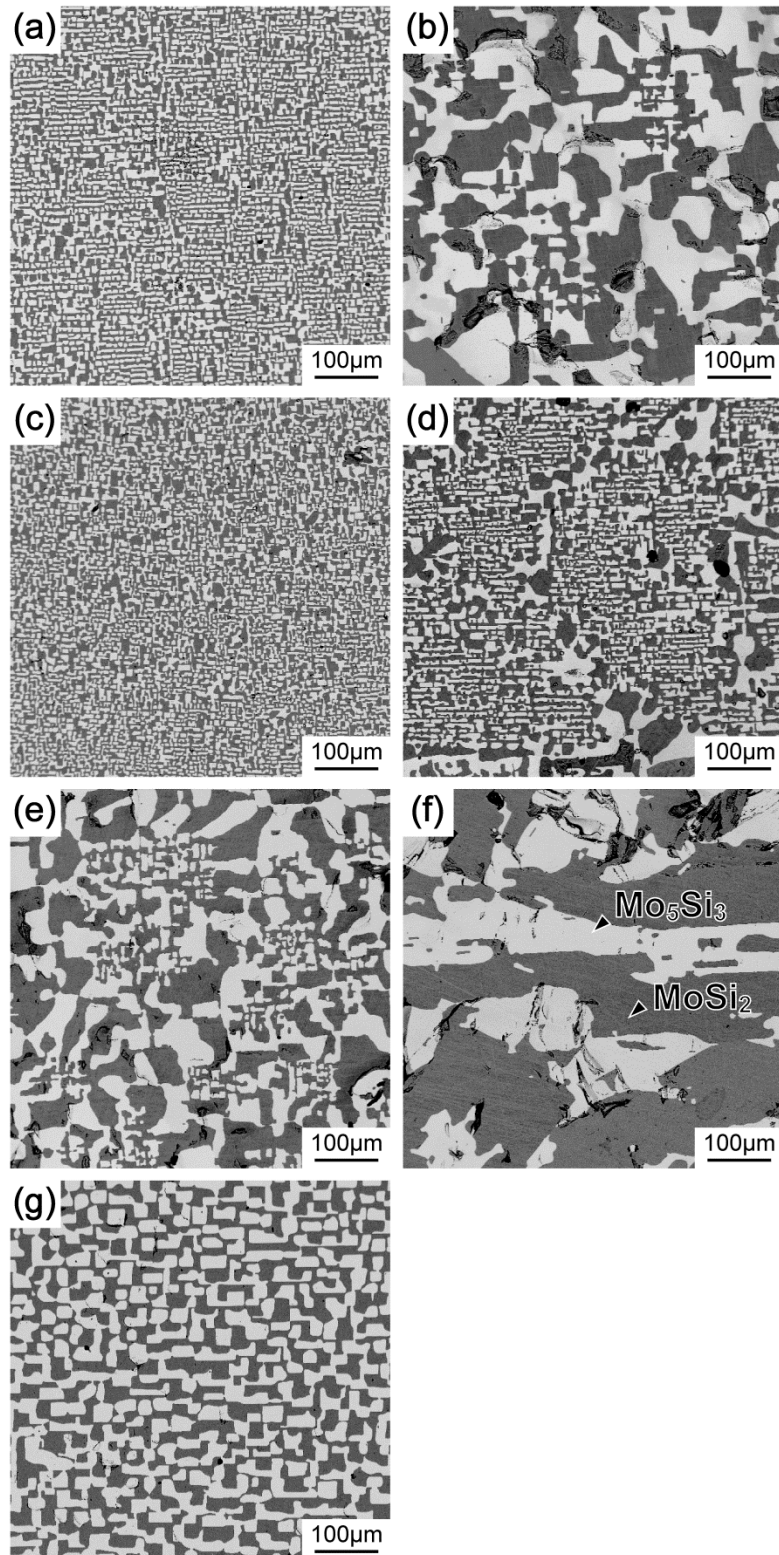


Fig. 5. SEM backscattered electron images of cross sections of DS $\text{MoSi}_2/\text{Mo}_5\text{Si}_3$ eutectic composites alloyed with (a) 1 at.% Ti, (b) 5 at.% Ti, (c) 2 at.% V, (d) 5 at.% V, (e) 1 at.% Cr, (f) 5 at.% Cr grown at a growth rate of 10mm/h and (g) 1 at.% Cr grown at a growth rate of 2 mm/h.

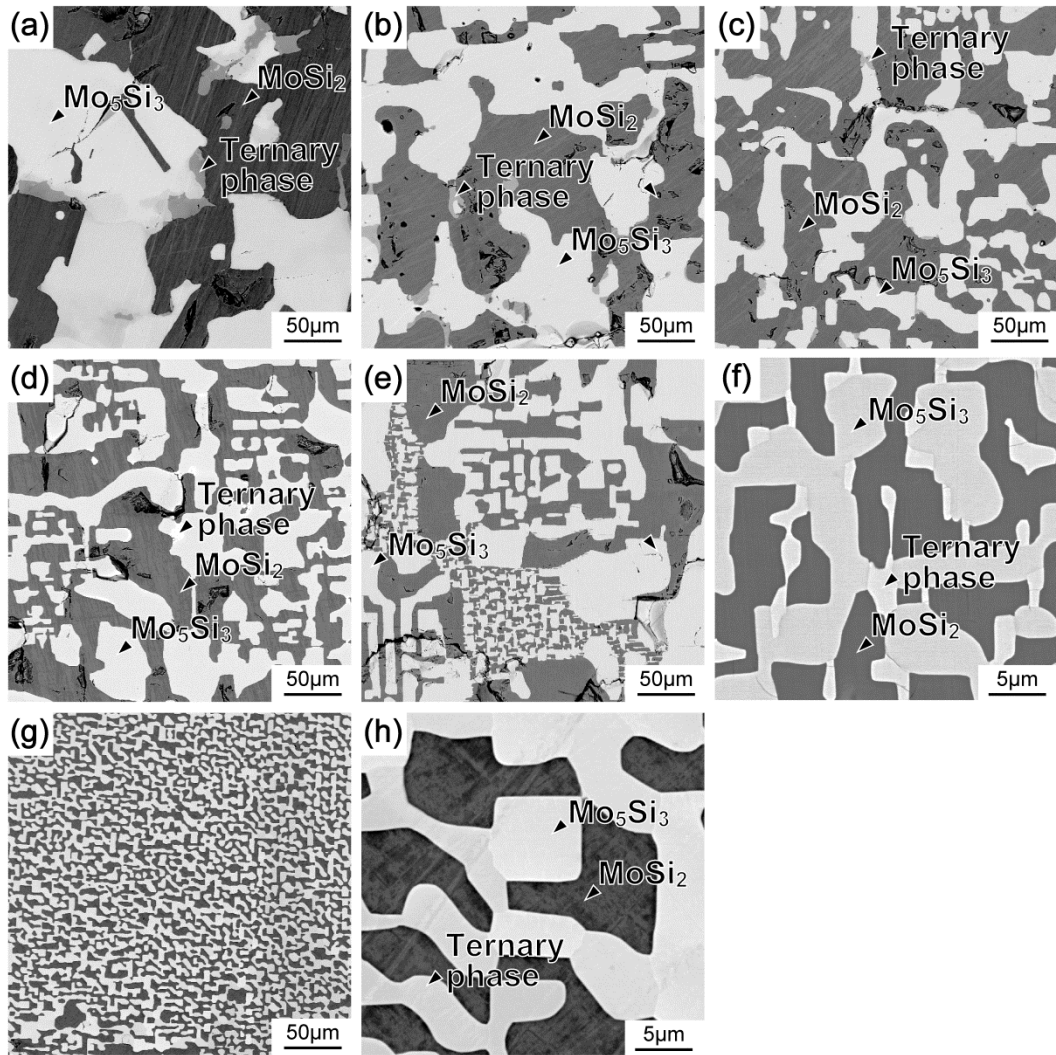


Fig. 8. SEM backscattered electron images of cross sections of DS $\text{MoSi}_2/\text{Mo}_5\text{Si}_3$ eutectic composites alloyed with (a) 2 at.% Fe, (b) 2 at.% Co, (c) 2 at.% Ni, (d) 0.2 at.% Ir, (e,f) 2 at.% B and (g,h) 1 at.% C grown at a growth rate of 10 mm/h.

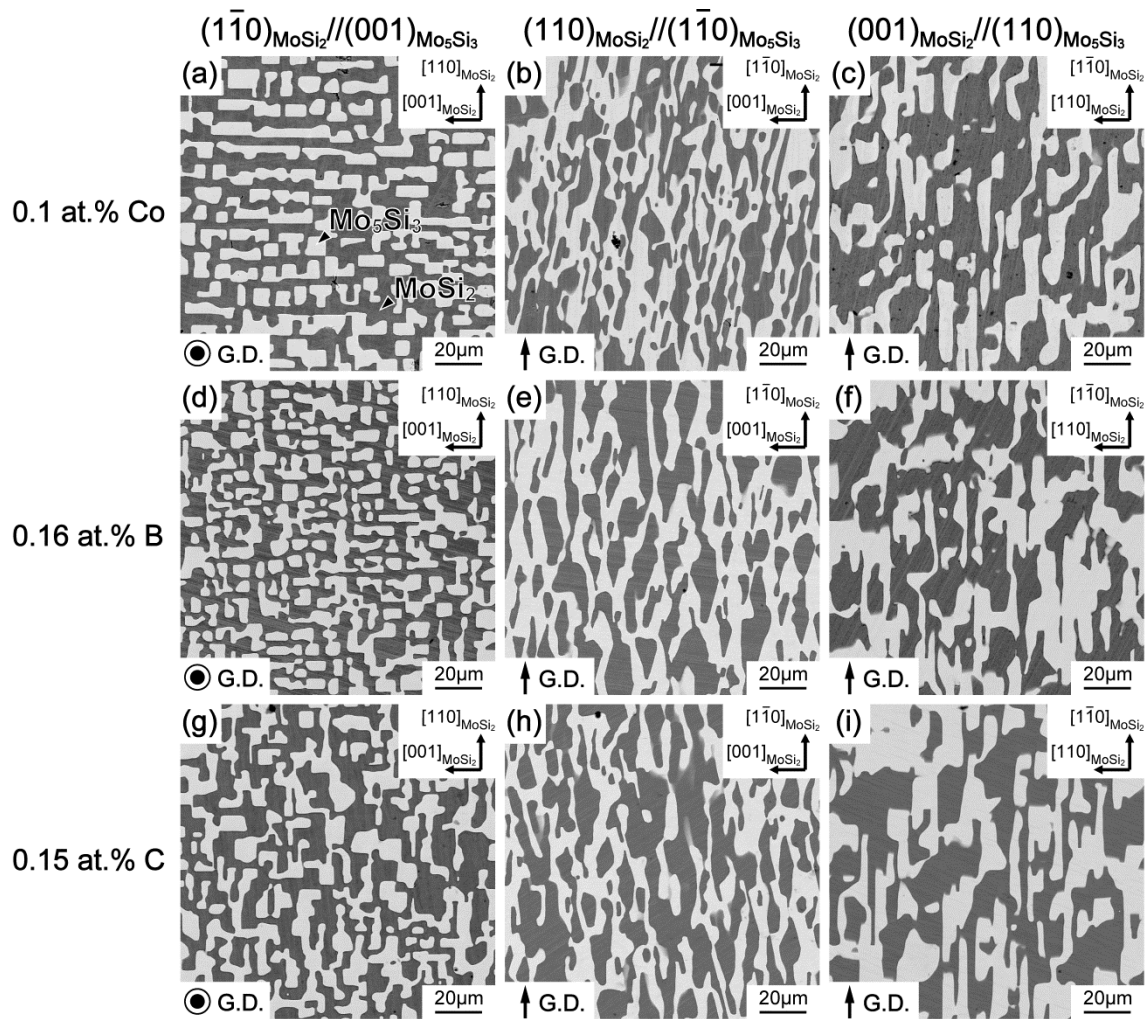


Fig. 9. SEM backscattered electron images of three mutually orthogonal sections of DS $\text{MoSi}_2/\text{Mo}_5\text{Si}_3$ eutectic composites alloyed with (a-c) 0.1 at.% Co, (d-f) 0.16 at.% (300 wt.ppm) B and (g-i) 0.15 at.% (300 wt.ppm) C grown at a growth rate of 10 mm/h.

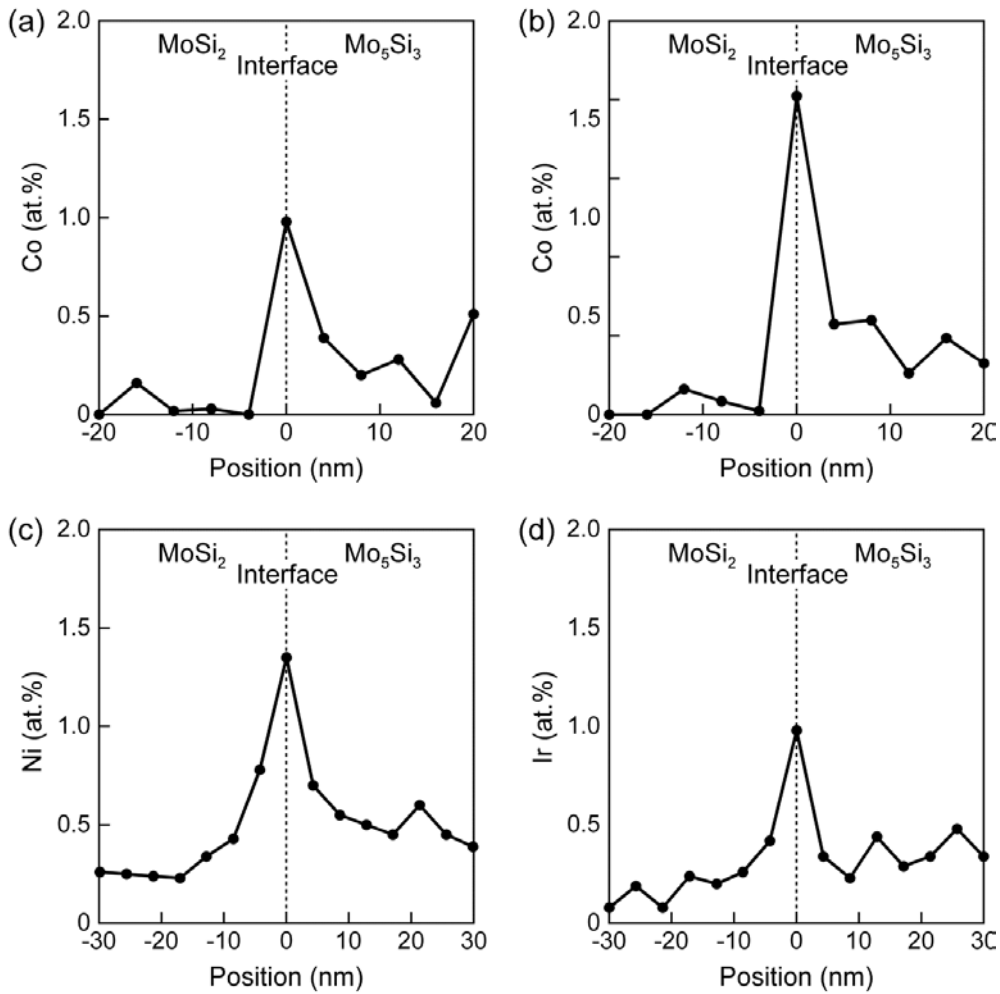


Fig. 10. Segregation behavior at (a) Interface I and (b,c,d) interface II interfaces in DS $\text{MoSi}_2/\text{Mo}_5\text{Si}_3$ eutectic composites alloyed with (a,b) 0.5 at.% Co, (c) 0.5 at.% Ni and (d) 0.2 at.% Ir.

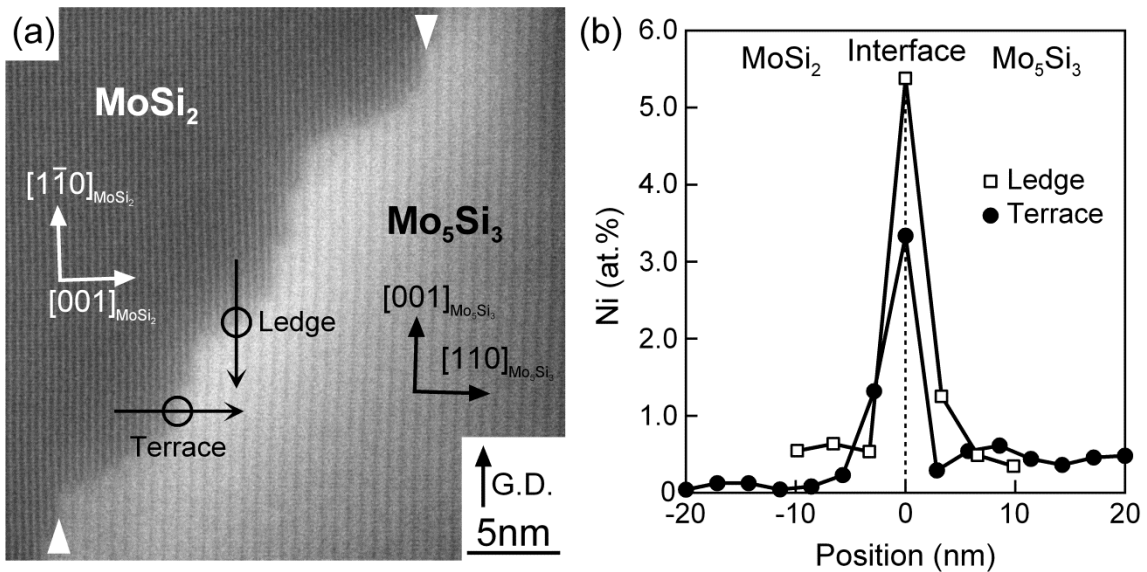


Fig. 11. (a) An atomic resolution HAADF-STEM image taken from the interface I in a DS ingot with 0.5 at.% Ni grown at a growth rate of 10 mm/h projected along $[1\bar{1}0]_{\text{MoSi}_2}/[110]_{\text{Mo}_5\text{Si}_3}$ and (b) segregation behavior at the ledge and terrace part of the interface I marked in (a).

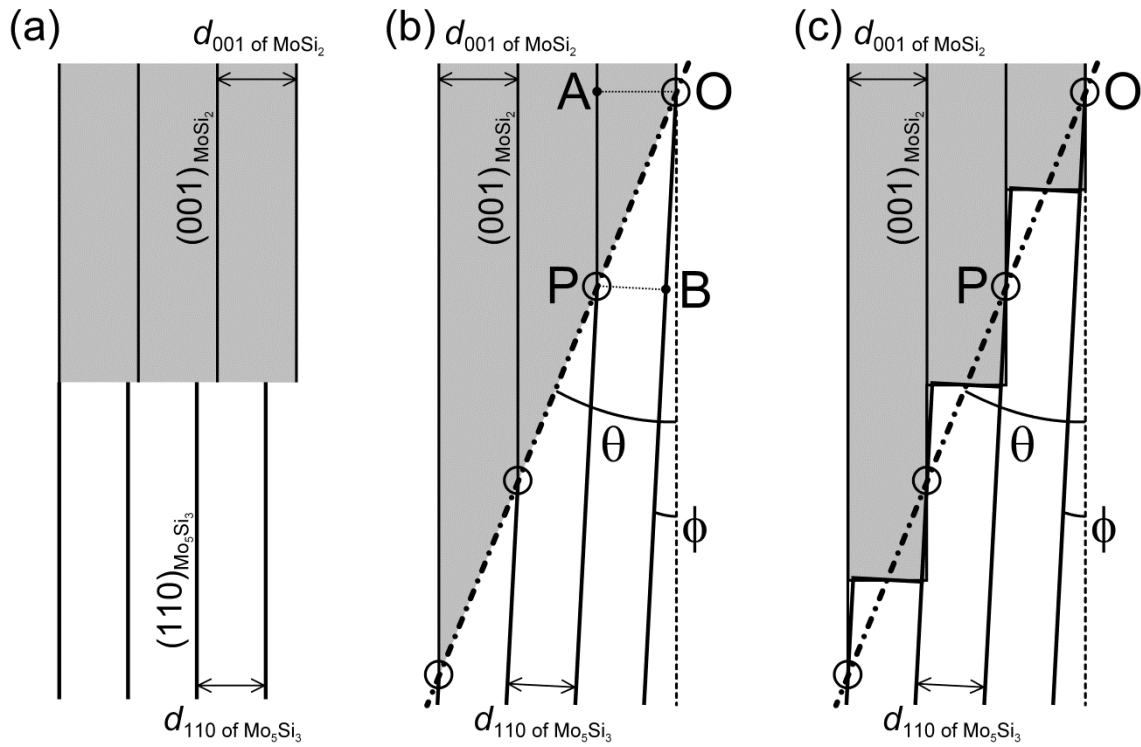


Fig. 12. Schematic illustration of macroscopic strain accommodation at interface I in the $\text{MoSi}_2/\text{Mo}_5\text{Si}_3$ DS eutectic composites.

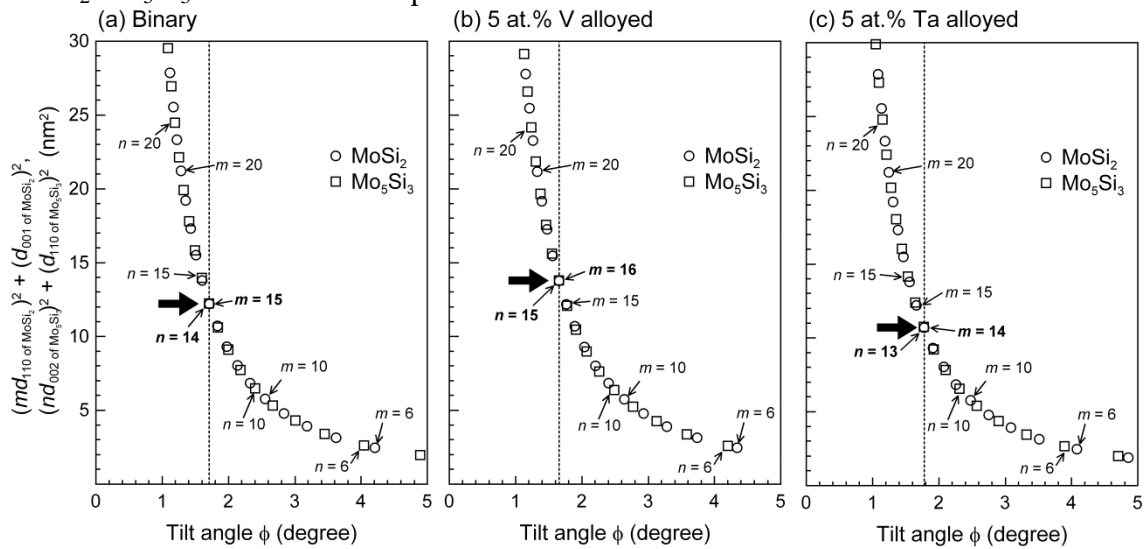


Fig. 13. Conditions for the macroscopic strain accommodation at the interface I estimated for $\text{MoSi}_2/\text{Mo}_5\text{Si}_3$ DS ingots of (a) binary, (b) 5 at.% V-alloyed and (c) 5 at.% Ta-alloyed materials.

Table 1. Chemical compositions and lattice constants for binary and ternary MoSi₂/Mo₅Si₃ eutectic composites alloyed with the type-1 elements.

Ternary element	Amount of addition	Phase	Chemical composition (at.%)			Lattice constants (nm)	
			Mo	Si	X	<i>a</i>	<i>c</i>
Binary	-	MoSi ₂	35.2	64.8	-	0.321	0.785
		Mo ₅ Si ₃	63.2	36.8	-	0.966	0.490
Ti atomic radius: 0.146nm	1	MoSi ₂	35.7	64.3	0.0	0.321	0.785
		Mo ₅ Si ₃	61.4	36.6	2.0	0.966	0.490
	5	MoSi ₂	35.6	64.4	0.1	0.321	0.785
		Mo ₅ Si ₃	53.9	36.8	9.3	0.968	0.490
V atomic radius: 0.135nm	2	MoSi ₂	35.2	64.6	0.2	0.321	0.785
		Mo ₅ Si ₃	58.7	37.1	4.2	0.964	0.488
	5	MoSi ₂	35.0	64.6	0.4	0.321	0.785
		Mo ₅ Si ₃	53.6	36.4	10.0	0.963	0.487
Cr atomic radius: 0.128nm	1	MoSi ₂	35.3	64.7	0.0	0.321	0.785
		Mo ₅ Si ₃	60.3	37.3	2.4	0.965	0.489
	2	MoSi ₂	35.6	64.4	0.0	0.321	0.785
		Mo ₅ Si ₃	59.3	37.6	3.1	0.964	0.488
	5	MoSi ₂	35.3	64.7	0.0	0.321	0.785
		Mo ₅ Si ₃	54.5	36.9	8.6	0.963	0.485
Nb atomic radius: 0.147nm	1	MoSi ₂	36.3	62.8	0.8	0.321	0.785
		Mo ₅ Si ₃	59.1	38.4	2.4	0.967	0.490
	2	MoSi ₂	36.5	62.5	1.1	0.321	0.785
		Mo ₅ Si ₃	57.7	37.2	5.1	0.968	0.491
	5	MoSi ₂	34.4	64.1	1.5	0.321	0.786
		Mo ₅ Si ₃	52.8	37.0	10.2	0.971	0.492
Ta atomic radius: 0.147nm	2	MoSi ₂	35.3	64.7	0.0	0.321	0.785
		Mo ₅ Si ₃	57.6	40.7	1.6	0.968	0.491
	5	MoSi ₂	34.7	65.3	0.0	0.321	0.785
		Mo ₅ Si ₃	48.7	45.8	5.5	0.971	0.493
W atomic radius: 0.141nm	1	MoSi ₂	35.4	58.7	5.8	0.321	0.786
		Mo ₅ Si ₃	57.1	37.8	5.1	0.966	0.490
	2	MoSi ₂	34.7	59.3	6.0	0.321	0.786
		Mo ₅ Si ₃	59.4	34.1	6.5	0.966	0.490
	5	MoSi ₂	33.0	58.6	8.4	0.321	0.786
		Mo ₅ Si ₃	55.7	32.2	12.1	0.965	0.491

Table 2. Chemical compositions for ternary MoSi₂/Mo₅Si₃ eutectic composites alloyed with the type-2 elements of Fe, Co, Ni and Ir.

Ternary element	Amount of addition	Phase	Chemical composition (at.%)		
			Mo	Si	X
Fe	2	MoSi ₂	35.4	64.6	0.0
		Mo ₅ Si ₃	61.1	37.1	1.8
		Ternary	35.3	38.0	26.7
Co	2	MoSi ₂	35.7	64.3	0.0
		Mo ₅ Si ₃	62.3	37.1	0.6
		Ternary	33.0	30.1	36.9
Ni	2	MoSi ₂	35.7	64.3	0.0
		Mo ₅ Si ₃	62.7	36.9	0.5
		Ternary	35.0	32.4	32.6
Ir	0.2	MoSi ₂	36.4	62.2	1.4
		Mo ₅ Si ₃	62.7	34.6	2.7
		Ternary	5.8	43.0	51.2